Thiol-Capped ZnO Nanowire/Nanotube Arrays with Tunable Magnetic Properties at Room Temperature

Su-Zi Deng,[†] Hai-Ming Fan,[‡,*] Miao Wang,[§] Min-Rui Zheng,[⊥] Jia-Bao Yi,[‡] Rong-Qin Wu,[⊥] Hui-Ru Tan,[∥] Chorng-Haur Sow,[⊥] Jun Ding,[‡] Yuan-Ping Feng,[⊥] and Kian-Ping Loh[†,*]

[†]Department of Chemistry, National University of Singapore, 3 Science Drive 3, Singapore 117543, [‡]Department of Materials Science and Engineering, National University of Singapore, Faculty of Engineering, 7 Engineering Drive 1, Singapore 117574, [§]Singapore—MIT Alliance, E4-04-10, 4 Engineering Drive 3, Singapore 117576, [⊥]Department of Physics, National University of Singapore, 2 Science Drive 3, Singapore 117542, and [∥]Institute of Materials Research and Engineering, 3 Research Link, Singapore 117602

ABSTRACT The present study reports room-temperature ferromagnetic behaviors in three-dimensional (3D)-aligned thiol-capped single-crystalline ZnO nanowire (NW) and nanotube (NT) arrays as well as polycrystalline ZnO NT arrays. Besides the observation of height-dependent saturation magnetization, a much higher M_s of 166 μemu cm^{-2} has been found in NTs compared to NWs (36 μemu cm^{-2}) due to larger surface area in ZnO NTs, indicating morphology-dependent magnetic properties in ZnO NW/NT systems. Density functional calculations have revealed that the origin of ferromagnetism is mainly attributed to spin-polarized 3p electrons in S sites and, therefore, has a strong correlation with Zn—S bond anisotropy. The preferential magnetization direction of both single-crystalline NTs and NWs lies perpendicular to the tube/wire axis due to the aligned high anisotropy orientation of the Zn—S bonds on the lateral (100) face of ZnO NWs and NTs. Polycrystalline ZnO NTs, however, exhibit a preferential magnetization direction parallel to the tube axis which is ascribed to shape anisotropy dominating the magnetic response. Our results demonstrate the interplay of morphology, dimensions, and crystallinity on spin alignment and magnetic anisotropy in a 3D semiconductor nanosystem with interfacial magnetism.

KEYWORDS: ZnO nanotubes and nanowires · thiol · magnetic properties · semiconductors

Nanomaterials possessing both ferromagnetic and semiconductor properties have attracted much attention in the past few years due to potential applications in wide ranging fields such as spintronics,[1] information storage,[2] and biomedicine.[3] III—V and II—VI diluted magnetic semiconductors are an attractive class of materials because spin-dependent magnetic phenomena can be potentially manipulated in the low dimensional tailored magnetic films for various spin-based devices. The traditional synthesis methods of dilute ferromagnetic semiconductors involve the doping of magnetic (nonmagnetic) elements into semiconductor nanoparticles to induce 3d—host hybridization and strong Coulomb interactions between 3d—3d electrons.[4] However, the nature and origin of the observed magnetic behavior of dilute magnetic semiconductors are still unclear. This is complicated by the presence of intrinsic point defects or extended defects which can also contribute to ferromagnetic behavior at room temperature in nondoped nanomaterials.[5−10]

Recently, organic passivation of noble metals to induce room-temperature ferromagnetism has been demonstrated in an organic—inorganic hybrid nanosystem.[11] For example, the permanent magnetic moment in thiol-capped Au nanoparticles at room temperature has been found and is associated with the spin of 5d localized holes as a result of Au—S bonding.[12] This phenomenon, termed interfacial magnetism, has stimulated the development of a new class of magnetic semiconductor nanostructures for various applications. Interfacial magnetic behavior has been observed for organically passivated semiconductor nanostructures including ZnO,[13] CdSe,[14] and PbS nanoparticle assembly on GaAs.[15] Of these, ZnO is particularly attractive because of its ability to retain ferromagnetism at room temperature and the possibility of producing spin field-effect transistors and light-emitting diodes with circularly polarized light emission. Theoretical study has verified that, when ZnO nanostructures are capped with amine or thiol, hybridization between Zn 4s orbitals with S 3p orbitals induces charge redistribution, which causes the 2p electrons in O and 3p electrons in S sites to become spin-polarized.[16] Moreover, ferromagnetic-like behavior has also been reported at room temperature for thiol-capped Ag nanocluster/ZnO NWs[17] and Ag—$Zn_{0.9}Co_{0.1}O$ metal—semiconductor hybrid nanostructures.[18] Unfortunately, most

*Address correspondence to msefhm@nus.edu.sg, chmlohkp@nus.edu.sg.

Received for review October 3, 2009 and accepted December 11, 2009.

Published online December 22, 2009. 10.1021/nn901353x

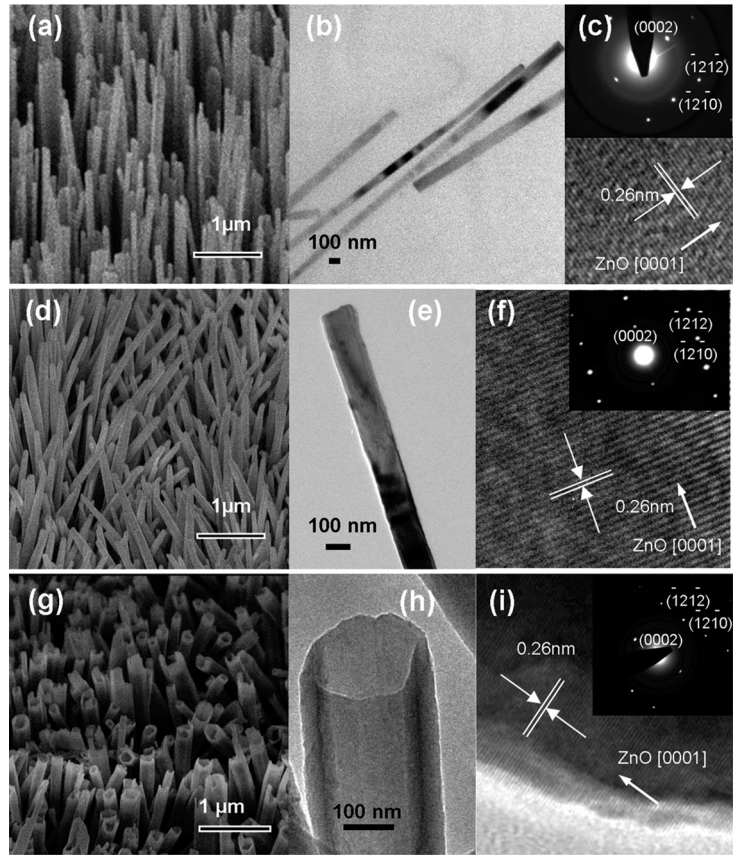

Figure 1. SEM and TEM of single-crystalline NWs and NTs: (a) 45° tilted SEM of vertically aligned VPT-grown NWs array; (b) TEM image of several VPT-grown NWs; (c) SAED and HRTEM of VPT-grown NW; (d) 45° tilted SEM of hydrothermally grown NW arrays; (e) TEM image of a single NW; (f) HRTEM of a single NW; inset shows the SAED pattern; (g) 45° tilted SEM of NT arrays, fabricated by etching of hydrothermally grown NW; (h) TEM of a single NT; (i) HRTEM of a single NT; inset shows the SAED pattern.

of these studies are limited to nanoparticle systems, in which the surfaces are multifaceted and the lack of long-range ordering of hybridized metal−S bonds leads to poor control over the magnetic properties. One-dimensional (1D) single-crystalline ZnO nanostructures such as nanotubes (NTs) and nanowires (NWs), possessing defined facets on the surface for ordered interfacial bond formation and an anisotropic geometry for the shape-tunable magnetic properties and polarized electron transport, are ideal candidates for addressing ferromagnetism in semiconductors by interfacial charge transfer across the semiconductor interface. In this way, the ferromagnetic organic−inorganic nanosystem can be extended from zero-dimensional (0D) thiol-capped ZnO nanoparticles to three-dimensional (3D) thiol-capped aligned ZnO NT and NW arrays. The additional degrees of freedom offered by NT/NW arrays by their geometry (*i.e.*, shape anisotropy) and alignment in the *z*-axis as well as the variation in diameter and wall thickness enable the modulation of the magnetic properties through the manipulation of the size, morphology, and crystallinity of the nanostructures. Thiol-capped ZnO NTs, with their moments arising due to charge transfer across the bond at the organic−inorganic interface, are expected to behave differently from typical ferromagnetic NTs. In addition, due to the higher specific surface and porosity, ZnO NTs are an attractive alternative to ZnO NPs and NWs for

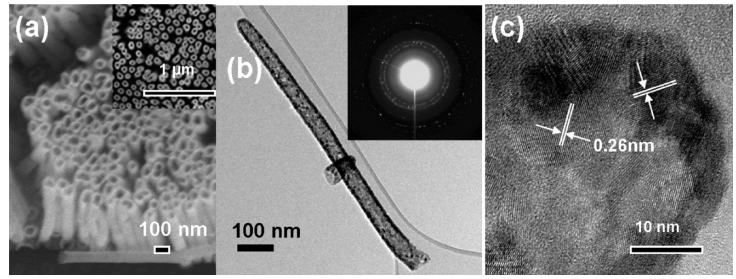

Figure 2. (a) SEM tilted view of ALD polycrystalline ZnO NT arrays; inset shows the top view. (b) TEM of a single polycrystalline NT, with SAED pattern in the inset, and (c) HRTEM of a single polycrystalline NT.

TABLE 1. Summary of Geometric Parameters of ZnO NWs and NTs, Synthesized by VPT, Hydrothermal Growth, and ALD

synthesis method	morphology	crystallinity	length (μm)	diameter (nm)	wall thickness (nm)	neighbor-to-neighbor distance (nm)
VPT	nanowire	single-crystalline	range from 4.1 to 15.5	80		133
hydrothermal	nanowire	single-crystalline	7	150		282
hydrothermal	nanotube	single-crystalline	4	294	30	411
ALD	nanotube	polycrystalline	1.5	80	15	104

the understanding of the effect of morphology on the physical properties of nanomaterials[19] and in the fabrication of new nanodevices.[20,21]

In the present work, we have developed an organic−inorganic 1D nanosystem consisting of an aligned array of thiol-capped ZnO NWs/NTs possessing room-temperature ferromagnetism. Vertically aligned single-crystalline and polycrystalline ZnO NWs/NTs were synthesized by vapor phase transport (VPT), hydrothermal treatment, and atomic layer deposition (ALD). Thiol molecules were self-assembled on the surface of ZnO NTs/NWs to induce charge transfer resulting in a magnetic moment across the thiol−ZnO interface. Density functional calculations are also performed to understand the origin of room-temperature ferromagnetism by considering the Zn−S bond geometry with respect to the lateral plane of the NW/NT. By comparison between single-crystalline and polycrystalline NWs and NTs, the correlations of dimensions, morphology, and crystallinity of these ZnO NWs/NTs on tunable magnetic properties were demonstrated.

RESULTS AND DISCUSSION

Characterizations of Bare and Thiol-Capped ZnO NWs/NTs. Aligned ZnO NW/NT arrays could be fabricated by various methods such as VPT, hydrothermal treatment, electrodeposition, and ALD. The ZnO NW/NT arrays obtained by VPT usually have high vertical alignment, while the hydrothermal treatment is a more facile method for the synthesis of ZnO NTs. Both methods can achieve large-scale growth of ZnO NW/NT arrays with single-crystalline nature. In contrast, the ZnO NWs/NTs prepared by template-based routes, for example, electrodeposition and ALD in anodic alumina oxide (AAO), generally result in polycrystalline ZnO NWs/NTs.[22] For the sake of comparison, we employed VPT, hydrothermal treatment, and ALD methods to synthesize ZnO NW/NT arrays with different dimensions and crystallinity in the current work.

The morphology and structure of vertically aligned ZnO NW/NT arrays were examined with scanning electron microscopy (SEM), transmission electron microscopy (TEM), and X-ray diffraction (XRD). Part a of Figure 1 shows the 45° tilted view SEM image of the ZnO NW arrays grown by VPT. The average diameter of the NWs is about 80 nm, and the density of the ZnO NW array is ~6.4 × 10^9/cm^2. The TEM image in part b of Figure 1 shows several NWs removed from the substrate. The selective-area electron diffraction (SAED) in part c of Figure 1 indicates the single-crystalline nature of the VPT-grown NWs. The SEM images of the ZnO NWs and NTs synthesized by hydrothermal method are presented in parts d−i of Figure 1. Parts d−f of Figure 1 show the 45° tilted SEM image, TEM image, and high-resolution TEM (HRTEM) image (with SAED in the inset) for the hydrothermally grown NWs of outer diameter ~150 nm, while parts g−i of Figure 1 show that for the NTs of outer diameter ~300 nm. The 45° tilted SEM views for the NW and NT in parts d and g of Figure 1 show the vertical alignment of the NWs and NTs. The TEM image of a single NT in part h of Figure 1 clearly shows the hollow structure of the NTs with well-defined traversal contrast, and the inner/outer wall surfaces are quite smooth. The 300 nm NTs have a wall thickness (d_{wall}) of ~30 nm. Similar to the VPT grown NWs, these hydrothermal grown NWs and NTs also show the single-crystal character, as shown in the HRTEM image and the SAED pattern in the insets shown in parts f and i of Figure 1. The SAED pattern is attributed to the hexagonal ZnO with zone axis [21−30]. For all single-crystalline NWs and NTs, the [0001] is the growth direction, and the side surfaces of the tube are formed by the equivalent (1000) family planes. ZnO NTs obtained by the facile solution procedures tend to be well-crystallized at a relatively low temperature, and the crystallinity of the obtained NTs is not affected by the selective dissolution of the NW core.

Parts a−c of Figure 2 show SEM and TEM images of the polycrystalline ALD ZnO NTs (after removal of the AAO template). The height of the template is 1.5 μm, and the interpore distance of the AAO template is around 100 nm, as shown in Figure 2a. The AAO pore size is reduced to 50−55 nm by the ZnO embedded

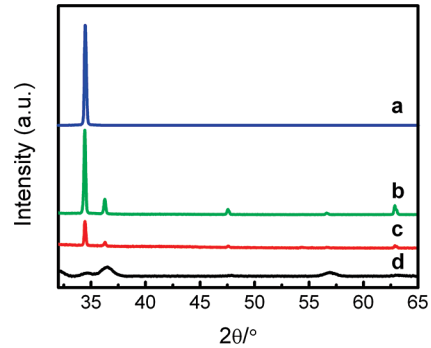

Figure 3. XRD patterns of ZnO NWs and NTs: (a) VPT-grown single-crystalline ZnO NWs, (b) hydrothermally grown single-crystalline NWs, (c) NTs fabricated by etching of hydrothermally grown NWs, and (d) polycrystalline ALD NTs.

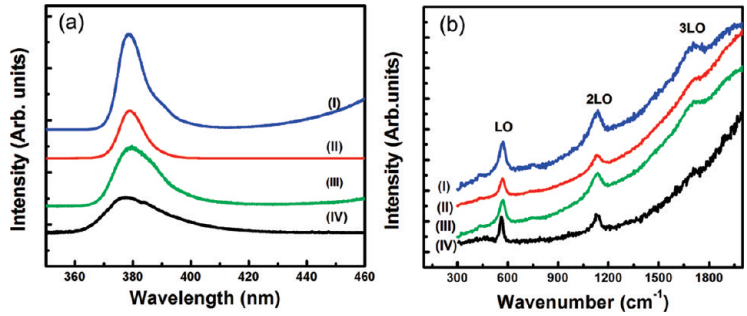

Figure 4. (a) Photoluminescence and (b) UV-Raman spectra of ZnO NW and NT arrays for (i) single-crystalline ZnO NWs fabricated by VPT, (ii) single-crystalline hydrothermally grown NWs, (iii) NTs fabricated by etching hydrothermally grown NWs, and (iv) polycrystalline ALD NTs.

onto the wall of pores, and the ZnO NTs produced have an average outer diameter of 80 nm with a wall thickness of ~15−20 nm for 100 ALD cycles. Figure 2b is a TEM image of a single NT which shows that the wall of the NT is uniform in thickness, confirming that successive ALD preserves the porous structure of the AAO template. The polycrystalline nature of the walls was confirmed by high-resolution TEM and SAED, as shown in Figure 2b,c. The bottom of the NT is closed due to ALD occurring on the underlying substrate; thus the contribution of thiol-capped Au to the measured magnetic signal can be ruled out, although the AAO is grown on a gold-coated Si. The geometric parameters of ZnO NWs and NTs are summarized in Table 1, providing an overview of the fabrication methods, crystallinities, and dimensions (length, diameter, neighbor-to-neighbor distance, and wall thickness).

The XRD patterns of ZnO NWs and NTs can be indexed as hexagonal ZnO, consistent with the values in the standard card (JCPDS 36-1451), and no impurity was observed as shown in Figure 3. For the single-crystalline NWs/NTs, they have a strong (002) orientation, but the ALD-deposited ZnO NTs are polycrystalline in structure.

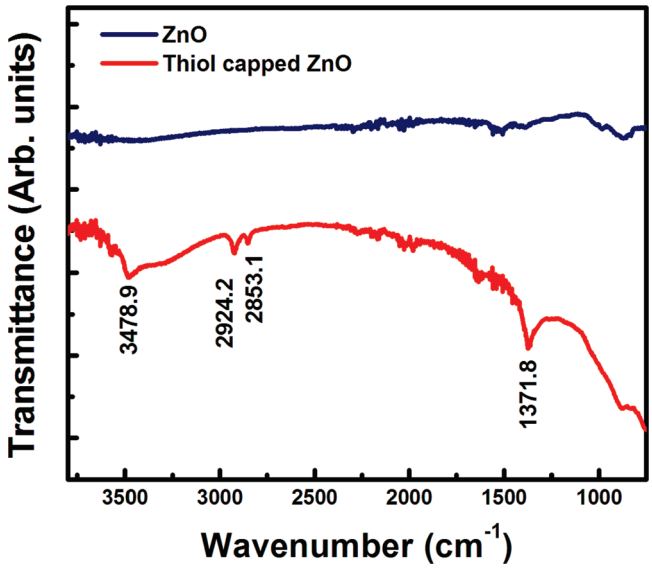

Figure 5. Typical infrared spectra of ZnO NTs and thiol-capped ZnO NTs.

The photoluminescence (PL) and resonance UV Raman spectra of as-prepared ZnO NWs/NTs are shown in Figure 4. As can be seen in Figure 4a, the peak at ~378 nm is observed for all samples, which is attributed to recombination of free exciton at the ZnO band edge. The slight blue-shifted peak of the polycrystalline NTs is due to finite size effect induced by smaller particle size.[23] By comparison with single-crystalline ZnO NWs, the broadening of the emission peak for ZnO NTs fabricated by hydrothermal method and polycrystalline NTs can be ascribed to defect-induced changes in electronic structure and its size heterogeneity (only for polycrystalline ZnO NTs). Resonance UV-Raman spectra for ZnO NWs and NTs are presented in Figure 4b. Three peaks at 571, 1135, and 1705 cm^{-1}, prominent in the measured region, correspond to the LO phonon (A_1 mode) and its overtones (nLO, n = 2,3).[24] Similar to the PL results, the Raman peak of polycrystalline ZnO NTs shows a slight blue shift due to their small particle size. The PL and resonance UV-Raman results indicate the good quality of obtained ZnO NW/NT arrays.

The obtained ZnO NWs and NTs were capped by thiol molecules by a self-assembly process. To confirm the existence of the thiol on the surface of ZnO NWs/NTs after the self-assembly process, infrared spectroscopy (IR) and X-ray photoelectron spectroscopy (XPS) were carried out for the ZnO NT arrays before and after thiol capping. Figure 5 shows the typical FTIR spectra of bare ZnO and thiol-capped ZnO NTs. The peaks at 2853 and 2924 cm^{-1} are due to the symmetric and asymmetric CH_2 stretching modes, and the peak at 1371 cm^{-1} is assigned to the CH_2 wagging mode. A comparison of the XPS spectra recorded from the bare ZnO and thiol-capped ZnO NTs is shown in Figure 6. Figure 6a shows the XPS data of Zn $2p_{3/2}$ in ZnO and thiol-capped ZnO NTs. The peak of thiol-capped ZnO NTs was shifted toward a lower binding energy by about 0.5 eV (from 1022.7 to 1022.2 eV), implying that some of the Zn−O bonds had been transferred into Zn−S bonds. In Figure 6b, the S 2p peak was observed in the spectrum of thiol-capped ZnO NTs but not for the bare ZnO. The S 2p peak can be resolved into three components of binding energies of 162, 164, and 165 eV which are assigned to thiolates (Zn−S−) and unbound thiols

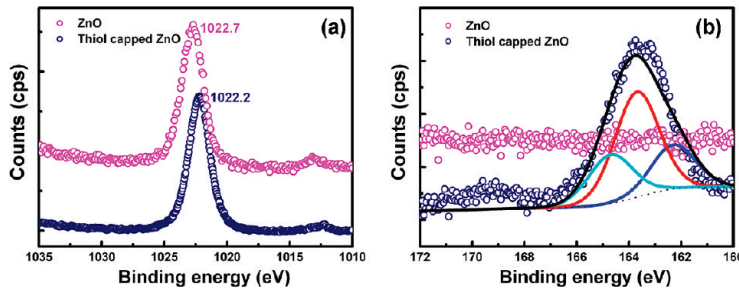

Figure 6. Typical Zn $2p_{3/2}$ (a) and S 2p (b) XPS spectra of ZnO NTs and thiol-capped ZnO NTs. The S 2p peak can be resolved into three components of binding energies of 162, 164, and 165 eV, which are assigned to thiolates (Zn−S−) and unbound thiols (−SH−) (with S $2p_{3/2}$ and S $2p_{1/2}$ components), respectively.

(−SH−) (with S $2p_{3/2}$ and S $2p_{1/2}$ components), respectively. The free thiols are attributed to the free end of 1,9-dodecanedithiol. The values of the Zn/S ratio on the surface of ZnO NWs/NTs have been estimated based on the Zn $2p_{3/2}$ component and thiolate Zn−S components of the S 2p peak. The calculated Zn/S atomic ratios are about 4.5 (VPT NW), 5.4 (hydrothermal NW), 2.8 (hydrothermal NT), and 2.1 (ALD NT) as listed in Supporting Information Table S1. These results clearly reveal that the ZnO NTs are effectively capped with the thiol.

Magnetic Properties of Thiol-Capped ZnO NWs/NTs. Most of the reports on room-temperature ferromagnetic properties of thiol or other organic molecule-capped ZnO nanostructures focused on nanocrystals or thin film.[25] In the case of 3D-aligned thiol-capped ZnO NW/NT arrays, the anisotropic geometry of the 1D nanostructure should result in a different amount of spins in the direction along the *z*-axis, depending on the height of the NW/NT. Hence, variations in M_s can also be controlled by varying the density or height of NWs or NTs on the substrate. Single-crystalline ZnO NWs grown by VPT were used to study the dependence of the magnetization on the heights of the NWs because it is easier to control the height of the NWs by controlling the growth time of ZnO. The cross-sectional SEM images in parts a−c of Figure 7 show that the NWs have a diameter of ~80 nm to with *c*-axis alignment and average heights of 4.1, 6.3, and 15.5 μm with growth times of 15, 30, and 60 min, respectively. Similar PLD−ZnO seed layers were used to grow these samples to ensure that the densities of NWs are similar for the three samples (~6.4 wires/μm^2). The hysteresis loops of the thiol-capped NWs of three different lengths are shown in Figure 7d, and the values of M_s are plotted against their heights in Figure 7e. The M_s of thiol-capped ZnO NWs increases noticeably with increasing length of the ZnO NWs. The height-dependent M_s of ZnO NWs clearly reveals that the M_s in such nanosystems can be tuned by controlling the height of the NWs. This is explicitly different from the interfacial magnetic properties of bulk thin film in which the thickness of the semiconductor thin

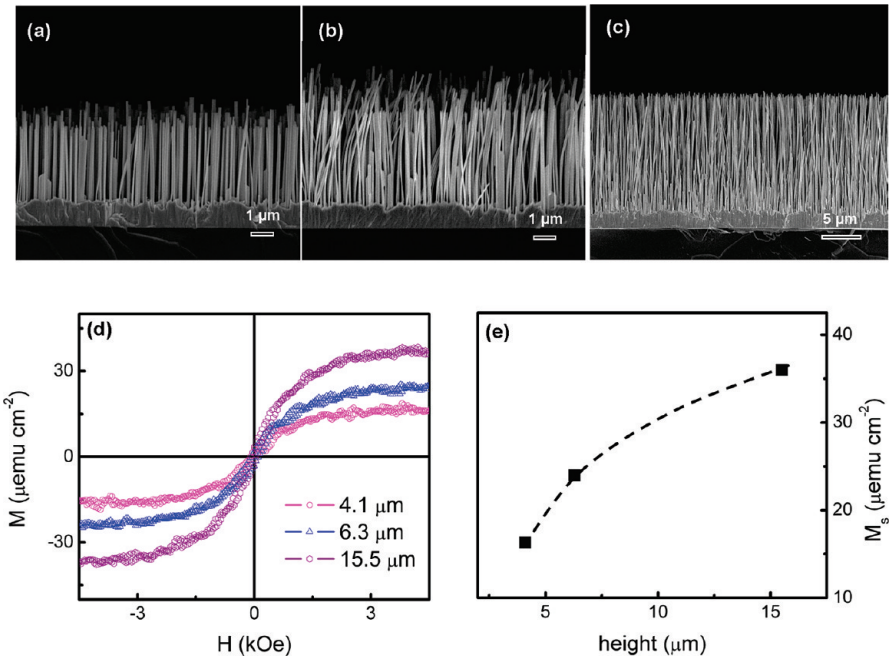

Figure 7. (a−c) Cross-sectional SEM images of ZnO NW arrays of different heights, grown by VPT for a duration of 15, 30, and 60 min, respectively. (d) Hysteresis loops of thiol-capped ZnO NWs of different heights. (e) Plot of saturation magnetization *vs* height of ZnO NWs.

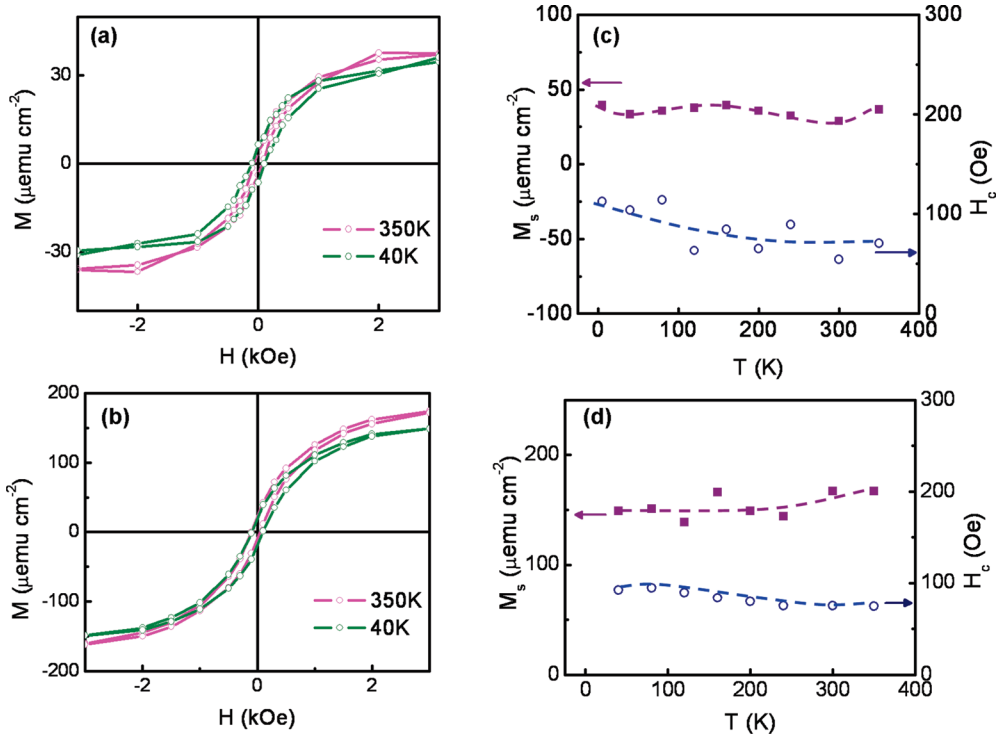

Figure 8. (a,b) Representative hysteresis loops for thiol-capped single-crystalline hydrothermally grown NW and NT arrays of diameters ~150 and ~300 nm, respectively, at 350 and 40 K, after subtraction of diamagnetic background signal. Temperature dependence of magnetization (M_s) and coercivity (H_c) measured for thiol-capped (c) NW and (d) NT arrays.

film would not affect their magnetic properties. In addition, it should be noted that all samples used here were examined by SEM, and statistical results of the NW density showed a narrow distribution below 13% (Supporting Information Figure S2); therefore, the possible effect of non-uniformity in NW density on the observed magnetic properties is negligible.

As the interfacial magnetism in ZnO nanostructures has a strong correlation with their surface area and dimension, it is of great interest to investigate the magnetic properties of NTs with respect to the NWs because of their unique hollow structure.[26] Even though the ZnO solid core does not play a role in the interfacial magnetic signal, the creation of the empty core is accompanied by the creation of an extra interface. To eliminate possible effect arising from the ZnO growth process, such as surface defects, which may affect the result of magnetic measurement, both NWs and NTs studied here were grown by hydrothermal method. Representative hysteresis curves obtained for thiol-capped 150 nm NWs and 300 nm NTs obtained at 350 and 40 K are shown in parts a and b of Figure 8. The magnetization curves for ZnO NWs/NTs before thiol capping indicate that the ZnO NWs/NTs are diamagnetic in the uncapped form (see Supporting Information Figure S3), and room-temperature ferromagnetism appears *ex nihilo* at the interface after the assembly of thiols on ZnO NWs/NTs. As can be seen in parts a and b of Figure 8, the M_s of thiol-capped ZnO NTs is 166 μemu cm^{-2}, much higher than the thiol-capped ZnO NWs (36 μemu cm^{-2}). The average heights of the NWs and NTs are estimated to be ~7 and ~4 μm from the cross-sectional view of SEM images, thus the possibility of the difference in height of the NWs or NTs as the main reason for the difference in M_s between the NTs and NWs could be ruled out. Instead, it is likely that the extra interface on the inner wall of the NT created by the etching process has increased the number of domains consisting of the Zn−S surface dipoles present on the surface of NTs relative to the NWs, as illustrated in the schematic in parts a and b of Figure 9. As the wall thickness for the NT becomes much smaller than the diameter of the NW, the surface-to-bulk atomic ratio increases for the NTs relative to the NWs. A high surface state density can significantly alter the chemical and physical properties of materials, which include changes in the charge distributions due to the finite size effect and quantum confinement of the electrons.[27−29] In addition to the physical increase in surface area in the NTs, the formation of tubes in this case possibly enhances the surface effect in 1D structures,[30] and this enables the interfacial ferromagnetism to offset the diamagnetic contribution of the bulk ZnO.[31,32] The enhanced M_s indicates that the strategy of the etching of NWs into NTs has proven to be an effective method for enhancing the interfacial ferromagnetic signal in the thiol-capped 1D ZnO nanostructures.

The variations of magnetization (M_s) and coercivity (H_c) with temperature for the thiol-capped NWs and NTs under ZFC conditions are shown in parts c and d

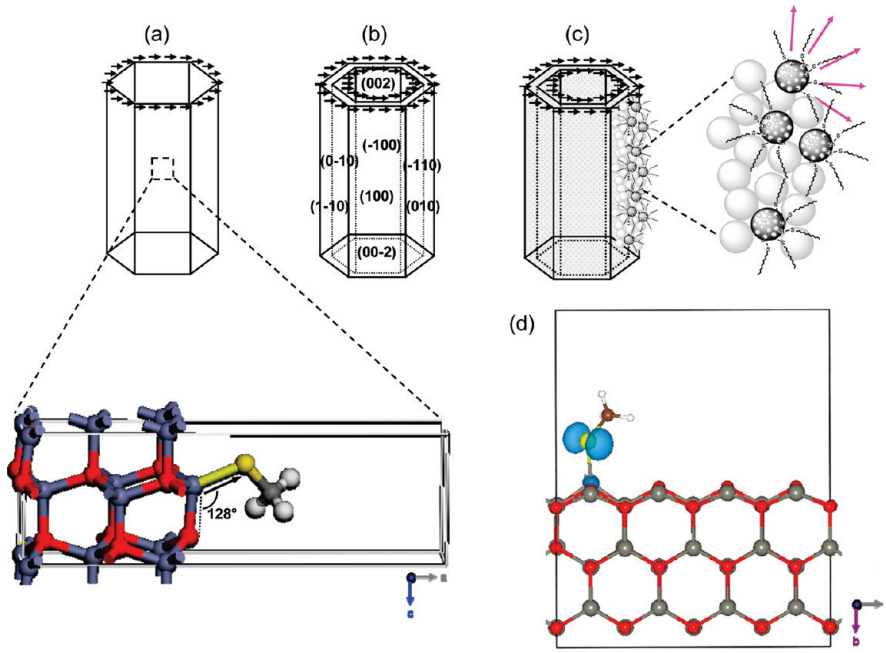

Figure 9. Schematics of the distribution of dipole moments on the lateral side walls and inner wall for thiol-capped single-crystalline (a) NW, (b) NT, and (c) polycrystalline NT, in the presence of a field applied in-plane (perpendicular to the NT axis). An extra layer of dipole moments is present on the inner surface of the hollow NT. Inset of a shows the zoom-in view of the interface of thiol−ZnO showing that −SH bonded to the (100) side plane of the hexagonal ZnO NW/NT at an angle of 128°. Gray atoms represent Zn; red atoms O; yellow atoms S; white atoms H. Unaligned spins lead to randomly distributed dipole moments on polycrystalline facets in (c). (d) Isosurface of spin distribution of S−CH_3 residue on ZnO (200) at the level of 0.00002/Å. Zn is in gray, O in red, S in yellow, C in chocolate, and H in white.

of Figure 8, respectively. The persistence of an almost invariant M_s and H_c, over a broad interval between 5 and 350 K in both the NTs and NWs, is a clear signature of interfacial magnetism. The magnetic moment is a result of orbital momentum at the surface conduction electrons induced by a localized charge and/or spin through spin−orbit interaction. The strong effective spin−orbit field, H^*, acting between the localized spin and the induced orbital momentum of the conduction electrons, leads to extremely high local magnetic anisotropy that blocks the moments from switching and is responsible for the absence of thermal fluctuation effects.[33] In addition, the thermally independent magnetization also rules out magnetic impurities as the origin of the magnetic properties of ZnO NTs as magnetic impurities dispersed in a nonmagnetic matrix results in the magnetization decreasing with temperature. The finite H_c, M_r, and saturating magnetic signals as seen from the $M-H$ curves measured at 300 K confirmed the room-temperature ferromagnetism of ZnO NTs. From ZFC−FC curves of the thiol-capped ZnO NT arrays, a Curie temperature close to 350 K can be obtained for the thiol-capped NTs (Supporting Information Figure S5).

When thiols interact strongly with ZnO to form close-packed self-assembled monolayers (SAMs),[34] surface electrons orbit around the nanometric to micrometric self-assembled domains to induce giant anisotropic orbital momenta, with long-range ordering of the magnetic dipoles possible on the aligned NT/NW arrays.[35] Figure 9a−c is a schematic of the distribution of dipole moments on the lateral side walls and inner walls for the thiol-capped single-crystalline and polycrystalline ZnO NWs and NTs. The optimized structure shows that the Zn−S bond forms an angle of ~128° with the (100) plane for the thiol-capped single-crystalline ZnO NWs and NTs, as shown in the inset of Figure 9a. To explore the possible origin of the observed magnetism, we performed *ab initio* density functional calculation on the S−CH_3 residue adsorbed to the ZnO (100) surface using VASP code.[36] Six (100) layers were used to model the infinite plane with in-plane periodicity of 12.997 × 10411 Å (from theoretical optimized equilibrium geometry). Atoms in the two layers at the bottom were fixed, while all other atoms were relaxed with a force tolerance of 0.05 eV/Å. Ultrasoft pseudopotential was used to represent the ion electron (or spin) interactions. The generalized gradient approximation[37] was adopted for exchange-correlation function. The wave function was expanded in plane waves with a cutoff energy of 520 eV, and the Brillouin zone is sampled by (0,0,0) *k*-point. The result suggested a finite spin polarization with net spin localized on the S atom of the S−CH_3 residue, as indicated in Figure 9d. The total spin was 0.67 μ_B, with 0.62 μ_B from S atom and 0.07 μ_B from an O atom in the vicinity of Zn. The relaxed S−Zn and S−C bond lengths are 2.32 and 1.82 Å, respectively. From the shape of the spin distribution, the net spin is mainly from the 3p electrons of S atom with a magnetic moment oriented perpendicular to the (200) surface of ZnO. The

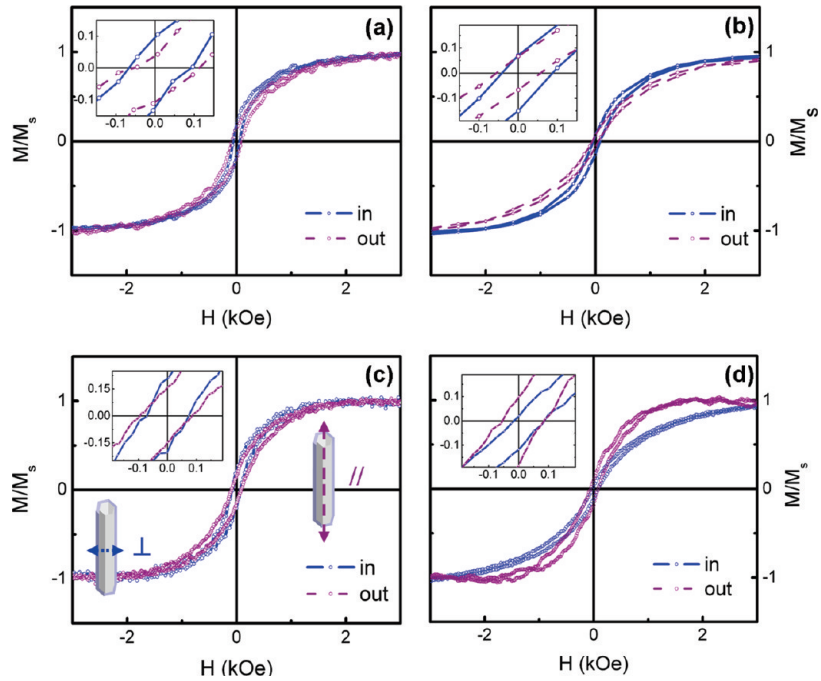

Figure 10. Normalized in-plane (perpendicular to tube axis) and out-of-plane (parallel to tube) hysteresis curves for thiol-capped (a) VPT-grown single-crystalline ZnO NWs, (b) hydrothermally grown single-crystalline NWs, (c) NTs fabricated by etching hydrothermally grown NWs, and (d) polycrystalline ALD NT arrays. In-plane and out-of-plane directions are defined with respect to the plane being the substrate on which the NWs/NTs were grown ("in" refers to applied magnetic field in the direction perpendicular to tube axis, while "out" refers to applied magnetic field in direction parallel to tube axis). Zoom-in views of the hysteresis curves near the origins are provided in the insets.

calculation result indicates a plausible origin of the observed room-temperature ferromagnetism. Furthermore, as the magnetism originates from S sites, the result also suggests that the magnetic properties would be strongly affected by the Zn−S bond geometry and their assembly.

In order to understand the possible magnetic anisotropy in thiol-capped ZnO NW and NT array systems induced by long-range ordering of the dipoles, in-plane and out-of-plane magnetic measurements of the thiol-capped NTs and NWs were carried out by alternating gradient magnetometry (AGM). The normalized magnetization curves for single-crystalline VPT-grown 80 nm NWs, hydrothermally grown 150 nm NWs, 300 nm NTs, and polycrystalline 80 nm NTs are shown in parts a−d of Figure 10, after subtracting the diamagnetic background. The insets in Figure 10c show the directions of applied magnetic field with respect to the NT geometry for in-plane and out-of-plane measurements. The values of remanance (M_r/M_s), magnetization (M_s), and coercivity (H_c) in the in-plane and out-of-plane directions for the thiol-capped NWs and NTs are summarized in Table 2. The coercivities (H_c) of the NWs/NTs in two directions, both parallel and perpendicular to the tube or wire axis, occur in the range of 50−91 Oe and do not show significant morphology or crystallinity dependence. As for the single-crystalline ZnO NWs and NTs, the magnetization curves obtained exhibited a similar easy axis in the in-plane direction. This is different from the observations in ferromagnetic Co NWs/NTs, in which the Co NW exhibits a sharper magnetization reversal than the Co NT when applied field is parallel to the direction of the tube axis, attributed to more rapid domain nucleation and propagation in the case of Co NWs than Co NTs.[38] Since the spins are located at the surface, the core of the thiol-capped ZnO NW does not participate in the magnetization process. In addition, magnetization reversal of ZnO NTs should exclude the transverse mode where a net magnetization component appears inside the wall, which is applicable for bulk ferromagnetic NTs.[39] Hence, the resemblance between the magnetization curves for thiol-capped single-crystalline ZnO NTs and NWs is not unexpected as the ferromagnetic signal for the thiol-capped ZnO NTs/NWs only arises at the interface.

However, the polycrystalline ZnO NTs exhibit an easy axis in the out-of-plane direction different from the single-crystalline NWs and NTs. According to the normalized magnetization curves for the single-crystalline and polycrystalline NWs and NTs, the saturation field of the single-crystalline ZnO NWs/NTs is lower for applied field perpendicular to the tube axis than in

TABLE 2. Summary of M_r/M_s, M_s, and H_c for the Thiol-Capped ZnO NWs and NTs

	$M_r/M_{s,\perp}$	$M_r/M_{s,\parallel}$	M_s (μemu cm^{-2})	$H_{c,\perp}$ (Oe)	$H_{c,\parallel}$ (Oe)
VPT NW (6.3 μm)	0.12	0.07	25	80.0	83.2
hydrothermal NW	0.11	0.07	36	64.8	56.5
hydrothermal NT	0.21	0.15	166	72.3	90.9
ALD NT	0.07	0.14	154	50.2	70.1

the parallel direction. In contrast, the saturation field of the polycrystalline ZnO NTs is lower for applied field parallel to the tube axis than in the perpendicular direction, and the in-plane remanant squareness (M_r,$M_{s,\perp}$) is only 0.07, much lower than 0.21 for the single-crystalline 300 nm NTs, while out-of-plane remanant squareness (M_r,$M_{s,\parallel}$) of the polycrystalline NTs is 0.14, higher than the M_r,$M_{s,\perp}$ of 0.07. This change of magnetic anisotropy from a single-crystalline to a polycrystalline ZnO NT array should be mainly due to the change of the anisotropic orientation of the Zn−S bonds. The harder-to-saturate magnetic signal in the longitudinal direction for the single-crystalline NWs or NTs is consistent with the nature of orbital magnetism in this system: the rotation of the angular momenta with an applied external magnetic field would require the rotation of the electric charge distribution linked to the highly oriented Zn−S bond at the (200) surface of the NTs.[11] Since a mismatch of the spin direction with the magnetic field makes it more difficult to saturate the signal in the longitudinal direction, the preferential magnetization direction will be perpendicular to the NW/NT axis. This experimental observation matches the results of the DFT calculation. However, this long-range ordering of dipoles is intrinsically difficult in the case of thiol-capped ZnO polycrystalline NTs due to its rough surface and the disordered bond orientations, as shown in Figure 9c. Consequently, the polycrystalline ALD NTs do not possess long-range Zn−S dipole orientation on the lateral side walls (Figure 9c), thus shape anisotropy of the NTs has a more important contribution to the magnetic anisotropy. In addition, the effect of coupling between NWs/NTs *via* dipole−dipole interaction on magnetic anisotropic properties, which may be present in a collection of wires or tubes with inherent easy axis along their long axis and in close proximity to one another, can be ruled out. Due to the low magnetic moment and large spacing between the ZnO NWs/NTs, such coupling is relatively small, and magnetostatic interaction between the NWs and NTs in the array may be negligible. Furthermore, the observed dependence of the anisotropy on the orientation of the organic molecule relative to the surface normal is similar to that of PbS nanoparticles linked to GaAs surface by 1,8-octanedithiol and 1,4-benzenedimethanethiol[14] as well as thiol-capped gold surface.[33] This convergence of experimental observations highlights an interesting phenomenon; that is, well-defined crystal faces play an important role in the magnetic anisotropy contributed by interfacial spins at a SAM-modified interface. Although the magnetic anisotropy for different thiol-capped ZnO NW/NT arrays determined by remanant squareness is small, the results imply the possibility that, by implementing these interfaces on 1D nanostructures, the defined magnetization direction with respect to the 1D nanostructure axis may allow tuning of magnetic anisotropy depending on the alignment, dimensions, and crystallinity of the 1D nanostructures.

CONCLUSION

In summary, we have investigated magnetic properties of thiol-capped 3D single-crystalline ZnO NWs and NTs as well as polycrystalline ZnO NT arrays. Room-temperature ferromagnetism has been observed in these thiol-capped NW and NT arrays. A density functional calculation has been performed, and the result indicates that the magnetism in such a system mainly originated from the spin-polarized 3p electrons in S sites. The dependence of M_s of ZnO NW arrays on the NW height can be ascribed to a higher number of Zn−S bond spins formed at the ZnO−thiol interface. Similarly, the NTs exhibited a higher M_s than the NWs due to its larger surface-to-volume ratio and thus higher density of Zn−S bond spins. The observed dependence of the magnetic anisotropy on crystallinity of ZnO NTs suggests that the change in the ordering of Zn−S spins on the crystal facets can affect the extent of magnetic ordering and alter the preferred magnetization direction. The magnetic properties in aligned thiol-capped ZnO NW/NT systems are very complex, and many factors such as geometric parameters of ZnO NWs/NTs (length, diameter, wall thickness, neighbor-to-neighbor distances) and chemical effect of thiolate bond formation can affect the observed magnetic properties. However, the results indicate that the rational control of the magnetic properties by tuning the morphology and crystallinity of these 1D ZnO nanostructures can be achieved. The ability to tune the magnetic properties demonstrated here offers opportunities for the utilization of these ferromagnetic ZnO NW/NT arrays as nanoscale building blocks in optoelectronic and magneto-optical devices.

METHODS

Fabrications of ZnO NWs and NTs: Vertically aligned single-crystalline ZnO NW arrays were synthesized *via* vapor phase transport in a sealed horizontal tube furnace (Carbolite CTF 12/75/700). A 0.40 g powder mixture of ZnO (99.99%, Aldrich) and graphite (<20 μm, synthetic, Aldrich) in a weight ratio of 1:1 was placed at the bottom of a one-end-closed small quartz tube. A piece of Si(100) wafer predeposited with a 200 nm ZnO seed layer by PLD served as substrate and was placed nearer to the open end. The small quartz tube was inserted into the large alumina work tube. The furnace was initially evacuated to a base pressure of 2.0×10^{-2} mbar, before Ar carrier gas mixed with 0.25% O_2 by volume of a total flow rate of 80 sccm was flown. The pressure in the alumina work tube was raised to 2.0 mbar by partially closing a backing valve. The furnace was heated to 900 °C within 40 min and held at that temperature for 15, 30, and 60 min to synthesize ZnO NW arrays of various lengths. The local temperature at the Si substrate during the growth process was approximately 800 °C. After cooling to room temperature, the Si wafer covered with gray color was taken out for further analysis.

Aligned single-crystalline ZnO NW/NT arrays on Si or glass substrates were also grown using the hydrothermal method with precoated ZnO seed layers prepared by the hydrolysis of zinc salts.[40] The ZnO NW arrays grown on the substrates were rinsed with deionized water and transferred into 0.03−0.05 M ethylenediamine (EDA) aqueous solutions at 65−75 °C for a period of 5−18 h to etch the NWs into NTs. The obtained samples were rinsed with deionized water and ethanol several times and then dried with N_2 between rinses.

Polycrystalline ZnO NTs were fabricated by an atomic layer deposition (ALD).[41] Briefly, an anodized aluminum oxide (AAO) template, prepared on Si substrate by a two-step anodization,[42] was subjected to ALD in a commercial ALD system (f · XALD, Azimuth Technologies Pte. Ltd., Singapore). Two precursors, diethyl zinc (DEZn) and deionized water, were fed into the reaction chamber in turn carried by a flow of 200 sccm N_2 gas and purged by the N_2 nitrogen gas flow between every ALD cycle. The system background pressure was maintained at 0.6 Torr. The cycle of DEZn pulse−purging−H_2O pulse−purging was repeated for 100 cycles for a ZnO wall thickness of about 20 nm.

Self-Assembly of Thiol on ZnO NWs/NTs: In a typical process, the ZnO NW arrays on the substrates were immersed in 30 mL of 1 mM 1,9-nonanedithiol solution in ethanol for the thiol molecule to self-assemble on the ZnO. This was carried out in a glovebox with an inert atmosphere overnight, after which the thiol-capped NTs or NWs were rinsed with ethanol and dried with N_2. The thiol-capped NT arrays are processed in the same manner.

Characterizations of Bare and Thiol-Capped ZnO NWs/NTs: Deposited products were characterized and analyzed using X-ray diffraction (XRD, Bruker-AXS, Cu Kα (1.542 Å) radiation), field emission scanning electron microscopy (FESEM, JEOL JSM-6700F), and transmission electron microscopy (TEM, JEOL JEM-3010). Micro-PL and UV-resonance Raman spectra were measured by Renishaw Invia system with 325 nm excitation line at room temperature. FTIR analysis was performed in a Nicolet 380 FTIR spectrometer, equipped with DTGS detector and a ATR attachment (using a diamond crystal). X-ray photoelectron spectroscopy (XPS) was performed with a Phobios 100 electron analyzer (SPECS GmbH) using an unmonochromated Mg Kα X-ray source (1253.6 eV). The magnetic properties of the ZnO NW/NT arrays were measured by an alternating gradient magnetometer (AGM) with the field applied in the in-plane and out-of-plane direction. Low-temperature hysteresis loops were measured with a superconducting quantum interference device (SQUID, QUANTUM DESIGN) magnetometer. The sample sizes range from 3 × 3 to 5 × 5 mm. The as-measured hysteresis loop consists of a ferromagnetic signal superimposed on a diamagnetic background. The diamagnetic background was subtracted to display the ferromagnetic signal only.

Acknowledgment. K.-P.L. thanks MOE grant "Structure and Dynamics of Molecular Self Assembly Layer" R-143-000-344-112 for funding support. This work was also supported by the Ministry of Education (MOE) Academic Research Fund under Grant R284-000-056-281.

Supporting Information Available: XPS results for thiol-capped ZnO NWs and NTs. Statistical distribution of nanowire density of VPT-grown nanowires. Magnetization curves for ZnO NTs/NWs and ZnO film before and after thiol capping. ZFC−FC measurements of thiol-capped NT arrays. This material is available free of charge *via* the Internet at http://pubs.acs.org.

REFERENCES AND NOTES

1. Wolf, S. A.; Awschalom, D. D.; Buhrman, R. A.; Daughton, J. M.; von Molnár, S.; Roukes, M. L.; Chtchelkanova, A. Y.; Treger, D. M. Spintronics: A Spin-Based Electronics Vision for the Future. *Science* **2001**, *294*, 1488–1495.
2. Piramanayagam, S. N.; Aung, K. O.; Deng, S.; Sbiaa, R. Antiferromagnetically Coupled Patterned Media. *J. Appl. Phys.* **2009**, *105*, 07C118.
3. Lee, H.; Yu, M. K.; Park, S.; Moon, S.; Min, J. J.; Jeong, Y. Y.; Kang, H. W.; Jon, S. Thermally Cross-Linked Superparamagnetic Iron Oxide Nanoparticles: Synthesis and Application as a Dual Imaging Probe for Cancer *In Vivo*. *J. Am. Chem. Soc.* **2007**, *129*, 12739–12745.
4. Marianna, C.; Vincenzo, G.; Elvio, C.; Cinzia, G.; Fabia, G.; Enrique, F. P.; Miguel, A. G.; Liberato, M.; Roberto, C.; Pantaleo, D. C. Topologically Controlled Growth of Magnetic-Metal-Functionalized Semiconductor Oxide Nanorods. *Nano Lett.* **2007**, *7*, 1386–1395.
5. Schoenhalz, A. L.; Arantes, J. T.; Fazzio, A. Surface Magnetization in Non-Doped ZnO Nanostructures. *Appl. Phys. Lett.* **2009**, *94*, 162503.
6. Hong, N. H.; Sakai, J.; Brize, V. Observation of Ferromagnetism at Room Temperature in ZnO Thin Films. *J. Phys.: Condens. Matter* **2007**, *19*, 036219.
7. Wang, Q.; Sun, Q.; Chen, G.; Kawazoe, Y.; Jena, P. Vacancy-Induced Magnetism in ZnO Thin Films and Nanowires. *Phys. Rev. B* **2008**, *77*, 205411.
8. Venkatesan, M.; Fitzgerald, C. B.; Lunney, J. G.; Coey, J. M. D. Anisotropic Ferromagnetism in Substituted Zinc Oxide. *Phys. Rev. Lett.* **2004**, *93*, 177206.
9. MacManus-Driscoll, J. L.; Khare, N.; Liu, Y.; Vickers, M. E. Structural Evidence for Zn Intersititials in Ferromagnetic $Zn_{1-x}Co_xO$ Films. *Adv. Mater.* **2007**, *19*, 2925–2929.
10. He, Y.; Sharma, P.; Biswas, K.; Liu, E. Z.; Ohtsu, N.; Inoue, A.; Inada, Y.; Nomura, M.; Tse, J. S.; Yin, S.; Jiang, J. Z. Origin of Ferromagnetism in ZnO Codoped with Ga and Co: Experiment and Theory. *Phys. Rev. B* **2008**, *78*, 155202.
11. Garitaonandia, J. S.; Insausti, M.; Goikolea, E.; Suzuki, M.; Cashion, J. D.; Kawamura, N.; Ohsawa, H.; de Muro, I. G.; Suzuki, K.; Plazaola, F.; Rojo, T. Chemically Induced Permanent Magnetism in Au, Ag, and Cu Nanoparticles: Localization of the Magnetism by Element Selective Techniques. *Nano Lett.* **2008**, *8*, 661–667.
12. López-Cartés, C.; Rojas, T. C.; Litrán, R.; Martínez-Martínez, D.; de la Fuente, J. M.; Penadés, S.; Fernández, A. Gold Nanoparticles with Different Capping Systems: An Electronic and Structural XAS Analysis. *J. Phys. Chem. B* **2005**, *109*, 8761–8799.
13. Garcia, M. A.; Merino, J. M.; Pinel, E. F.; Quesada, A.; de la Venta, J.; González, M. L. R.; Castro, G. R.; Crespo, P.; Llopis, J.; González-Calbet, J. M.; *et al.* Magnetic Properties of ZnO Nanoparticles. *Nano Lett.* **2007**, *7*, 1489–1494.
14. Seehra, M. S.; Dutta, P.; Neeleshwar, S.; Chen, Y. Y.; Chen, C. L.; Chou, S. W.; Chen, C. C.; Dong, C. L.; Chang, C. L. Size-Controlled *Ex Nihilo* Ferromagnetism in Capped CdSe Quantum Dots. *Adv. Mater.* **2008**, *20*, 1656–1660.
15. Alexander, Z.; Gregory, L.; Sidney, R. C.; Ron, N. Adsorption-Induced Magnetization of PbS Self-Assembled Nanoparticles on GaAs. *Adv. Mater.* **2008**, *20*, 2552–2555.
16. Wang, Q.; Sun, Q.; Jena, P. Ligand Induced Ferromagnetism in ZnO Nanostructures. *J. Chem. Phys.* **2008**, *129*, 164714.
17. Deng, S.; Loh, K. P.; Yi, J. B.; Ding, J.; Tan, H. R.; Lin, M.; Foo, Y. L.; Zheng, M.; Sow, C. H. Room Temperature Ferromagnetism at Self-Assembled Monolayer Modified Ag Nanocluster−ZnO Nanowire Interface. *App. Phys. Lett.* **2008**, *93*, 193111.
18. Qiu, X.; Li, L.; Tang, C.; Li, G. Metal−Semiconductor Hybrid Nanostructure Ag−$Zn_{0.9}Co_{0.1}O$: Synthesis and Room-Temperature Ferromagnetism. *J. Am. Chem. Soc.* **2007**, *129*, 11908–11909.
19. Anna, M.; Teresa, V. S.; Li, G.; Tsang, S. C. Shape and Size Effects of ZnO Nanocrystals on Photocatalytic Activity. *J. Am. Chem. Soc.* **2009**, *131*, 12540–12541.
20. Li, Q. H.; Gao, T.; Wang, Y. G.; Wang, T. H. Adsorption and Desorption of Oxygen Probed from ZnO Nanowire Films by Photocurrent Measurements. *Appl. Phys. Lett.* **2005**, *86*, 123117.
21. Wang, Q.; Lin, C. L.; Yu, X. B.; Wang, T. H. Room-Temperature Hydrogen Storage Characteristics of ZnO Nanowires. *Appl. Phys. Lett.* **2004**, *84*, 124–126.
22. Li, L.; Pan, S. S.; Dou, X.; Zhu, Y.; Huang, X.; Yang, Y.; Li, G.; Zhang, L. Direct Electrodeposition of ZnO Nanotube Arrays in Anodic Alumina Membranes. *J. Phys. Chem. C* **2007**, *111*, 7288–7291.

23. Greyson, E. C.; Babayan, Y.; Odom, T. W. Directed Growth of Ordered Arrays of Small-Diameter ZnO Nanowires. *Adv. Mater.* **2004**, *16*, 1348–1352.
24. Liu, R. B.; Pan, A. L.; Fan, H. M.; Wang, F. F.; Shen, Z. X.; Yang, G. Z.; Xie, S. S.; Zou, B. S. Phonon-Assisted Stimulated Emission in Mn-Doped ZnO Nanowires. *J. Phys.: Condens. Matter* **2007**, *19*, 136206.
25. Liu, J. F.; Liu, E. Z.; Wang, H.; Su, N. H.; Qi, J.; Jiang, J. Z. Surface Magnetism in Amine-Capped ZnO Nanoparticles. *Nanotechnology* **2009**, *20*, 165702.
26. Sui, Y. C.; Skomski, R.; Sorge, K. D.; Sellmyer, D. J. Nanotube Magnetism. *Appl. Phys. Lett.* **2004**, *84*, 1525–1527.
27. Zhang, P.; Sham, T. K. X-ray Studies of the Structure and Electronic Behavior of Alkanethiolate-Capped Gold Nanoparticles: The Interplay of Size and Surface Effects. *Phys. Rev. Lett.* **2003**, *90*, 245502.
28. Liu, H.; Mun, B. S.; Thomton, G.; Isaacs, S. R.; Shon, Y. S.; Ogletree, D. F.; Salmeron, M. Electronic Structure of Ensembles of Gold Nanoparticles: Size and Proximity Effects. *Phys. Rev. B* **2005**, *72*, 155430–155434.
29. Nobusada, K. Electronic Structure and Photochemical Properties of a Monolayer-Protected Gold Cluster. *J. Phys. Chem. B* **2004**, *108*, 11904–11908.
30. Xing, Y. J.; Xi, Z. H.; Zhang, X. D.; Song, J. H.; Wang, R. M.; Xu, J.; Xue, Z. Q.; Yu, D. P. Nanotubular Structures of Zinc Oxide. *Solid State Commun.* **2004**, *129*, 671–675.
31. Dutta, P.; Pal, S.; Seehra, M. S.; Anand, A.; Roberts, C. B. Magnetism in Dodecanethiol-Capped Gold Nanoparticles: Role of Size and Capping Agent. *Appl. Phys. Lett.* **2007**, *90*, 213102.
32. Hori, H.; Teranishi, T.; Nakae, Y.; Seino, Y.; Miyake, M.; Yamada, S. Anomalous Magnetic Polarization Effect of Pd and Au Nano-Particles. *Phys. Lett. A* **1999**, *263*, 406–410.
33. Hernando, A.; Crespo, P.; García, M. A.; Pinel, E. F.; de la Venta, J.; Fernández, A.; Penadés, S. Giant Magnetic Anisotropy at the Nanoscale: Overcoming the Superparamagnetic Limit. *Phys. Rev. B* **2006**, *74*, 052403.
34. Ulman, A. Formation and Structure of Self-Assembled Monolayers. *Chem. Rev.* **1996**, *96*, 1533–1554.
35. Jiang, G.; Wang, L.; Chen, T.; Yu, H.; Chen, C. Preparation of Gold Nanoparticles in the Presence of Poly(benzyl ether) Alcohol Dendrons. *Mater. Chem. Phys.* **2006**, *98*, 76–82.
36. Kresse, G.; Hafner, H. *Ab Initio* Molecular-Dynamics for Liquid-Metals. *Phys. Rev. B* **1993**, *47*, 558–561.
37. Langreth, D. C.; Perdew, J. P. Theory of Nonuniform Electronics Systems 0.1. Analysis of the Gradient Approximation and a Gernalization that Works. *Phys. Rev. B* **1980**, *21*, 5469–5493.
38. Li, D.; Richard, S. T.; Gerd, B.; Lu, J. G. Template-Based Synthesis and Magnetic Properties of Cobalt Nanotube Arrays. *Adv. Mater.* **2008**, *20*, 4575–4578.
39. Escrig, J.; Bachmann, J.; Jing, J.; Daub, M.; Altbir, D.; Nielsch, K. Crossover between Two Different Magnetization Reversal Modes in Arrays of Iron Oxide Nanotubes. *Phys. Rev. B* **2008**, *77*, 214421.
40. Greene, L. E.; Law, M.; Goldberger, J.; Kim, F.; Johnson, J. C.; Zhang, Y.; Saykally, R. J.; Yang, P. Low-Temperature Wafer-Scale Production of ZnO Nanowire Arrays. *Angew. Chem., Int. Ed.* **2003**, *42*, 3031–3034.
41. Wang, M.; Gao, H.; Carl, V. T.; Lee, K. T.; Chua, S. J. Growth and Characteristics of ZnO Nanotube Arrays on Si Substrate by Atomic Layer Deposition in Anodic Aluminum Oxide. MRS 2008 Fall Symposium B 2008.
42. Masuda, H.; Satoh, M. Fabrication of Gold Nanodot Array Using Anodic Porous Alumina As an Evaporation Mask. *Jpn. J. Appl. Phys.* **1996**, *35*, L126–L129.